Biochimica et Biophysica Acta 1848 (2015) 67–75

Contents lists available at ScienceDirect

Biochimica et Biophysica Acta

journal homepage: www.elsevier.com/locate/bbamem

Size dependent disruption of tethered lipid bilayers by functionalized polystyrene nanoparticles

Ying Liu, R. Mark Worden *

Department of Chemical Engineering and Materials Science, Michigan State University, East Lansing, MI 48824, USA

ARTICLE INFO

Article history:
Received 28 May 2014
Received in revised form 8 September 2014
Accepted 29 September 2014
Available online 5 October 2014

Keywords:
Polystyrene nanoparticle
Lipid bilayer
Disruption
Electrochemical impedance
Clustering
Aggregation
Biomembrane

ABSTRACT

Molecular interactions between engineered nanomaterials (ENM) and biomembranes are not well understood. This study investigated the effects of particle size and surface functional group on polystyrene nanoparticles' (PNPs) potency for biomembrane disruption. Electrochemical impedance spectroscopy was used to measure changes in the electrical resistance (R_m) of a tethered bilayer lipid membrane BLM (tBLM) composed of 1,2-dioleoyl-*sn*-glycero-phosphocholine (DOPC) following PNP exposure. All PNPs tested triggered a decline in the R_m that could be described using an exponential-decay model. Statistical hierarchical clustering analysis of two model parameters (exponential rate constant and fractional loss of R_m) could distinguish between the PNPs based on both size and surface functional group. For COOH modified nanoparticles, 20 nm PNPs were more potent in reducing R_m than 100 nm PNP. However, for amidine modified nanoparticles, 120 nm PNPs were more potent in reducing R_m than 23 nm PNP. The COOH modified PNPs were more potent in reducing R_m than amidine modified PNP, which tended to aggregate following exposure to a tBLM. Ultra performance liquid chromatography–mass spectroscopy analysis suggested that the aggregation may have been triggered by DOPC that was removed from the tBLM by the amidine PNP.

1. Introduction

Engineered nanomaterials (ENM) have at least one dimension smaller than 100 nm and offer a broad range of desirable features, including an extremely large specific surface area and unique electronic, photonic and catalytic properties [1–4]. ENM have huge potential markets and are increasingly being used for cosmetics, sensors, drug delivery and diagnostics [1]. However, safety concerns arising from ENM exposure have been raised [5–7]. For example, polystyrene nanoparticles (PNPs) have been shown to activate ion channels (K^+ and Cl^-) when interacting with human airway epithelial cells, thereby interfering with signal-transduction pathways [8]. In addition, PNP having different sizes and surface functionalization can exhibit cytotoxicity by causing G1 phase delay and disrupting membrane integrity [9]. Cationic PNPs were shown to induce mitochondrial damage and ATP depletion [10].

Reviews of both in vitro [11] and in vivo [12] ENM toxicity studies have reported inconsistent results between laboratories, even when similar nanotoxicity assays were used on apparently identical ENM. Recent round-robin efforts to simultaneously conduct standardized experimental protocols in different labs [13,14] have provided insight into factors responsible for this variability. These factors include ENM aggregation, which is influenced by ENM interactions with components in the liquid medium (e.g., electrolytes) [15] and subtle differences in the physicochemical properties of the ENM tested. Such differences may result from variations in the ENM's synthesis, purification, storage, age, handling, delivery method, and exposure to constituents in the liquid medium [16]. For example, incubation of uncoated PNP with cell-culture medium can result in coagulation [17].

ENM typically must interact with biomembranes to cause biological effects [18]. Thus, an improved understanding of ENM–biomembrane interactions would advance efforts to develop ENM that have the desired biosafety and functional properties [3,19,20]. There are several possible ENM–biomembrane interaction modes, each of which could lead to a different toxicological outcome. The ENM could adsorb onto the biomembrane, become embedded within the membrane, remove lipid molecules from the membrane, penetrate through the membrane, etc. ENM–biomembrane interactions are influenced by the properties of both the biomembrane and the ENM. Key properties of the ENM include the size, shape, concentration, rigidity, surface charge, chemical functionalities, degree of hydrophobicity/hydrophilicity, and surface ligand arrangement [20]. Key biomembrane properties include the lipid composition, the fluidity, and the presence of membrane-associated proteins, carbohydrates, and microdomains (e.g., lipid rafts). The inherent complexity, heterogeneity, and variability of intact cell membranes make it difficult to test hypotheses about the mechanisms of ENM–biomembrane interactions. In contrast, the biomimetic approach of using a synthetic bilayer lipid membrane (BLM) having a known composition allows

* Corresponding author. Tel.: +1 517 353 9015; fax: +1 517 432 1105.
E-mail address: worden@egr.msu.edu (R. Mark Worden).

http://dx.doi.org/10.1016/j.bbamem.2014.09.014
0005-2736/

the biomembrane's properties to be precisely controlled, thereby facilitating mechanistic studies relevant to nanotoxicity [15].

Unsupported planar BLM have been widely used in electrophysiology research, but they are inherently fragile and require expensive equipment to measure dynamics of single pores in the BLM [15]. These disadvantages can be circumvented by using a tethered bilayer lipid membrane (tBLM), in which the BLM is chemically tethered to a surface (e.g., a gold electrode). The ion reservoir that is formed between the tBLM and underlying electrode [21] allows application of electrochemical impedance spectroscopy (EIS) [22,23] to characterize ion transport across the tBLM mediated by ion channels [22], pore-forming proteins [24], and nanomaterials [25]. In a recent study, we showed that EIS could be used to characterize biomembrane disruption by silica-core ENM and that the ENM-induced reduction in the tBLM's electrical resistance (R_m) varied with the silica particles' surface functional group [26].

The phospholipid 1,2-dioleoyl-*sn*-glycero-phosphatidylcholine (DOPC) is a major constituent of many biomembranes that readily forms BLM at room temperature, and is well suited to form biomimetic interfaces that mimic biomembranes [27]. PNPs are well suited as model ENM to elucidate ENM–biomembrane interactions. Key properties of PNP, such as size and surface functionalization, can readily be customized. PNPs have been investigated for a wide range of commercial applications including drug delivery, food additives and other pharmaceutical implementations [28–30]. Transcellular trafficking of positively charged, amidine-modified PNP (amidine PNP) across primary rat alveolar epithelial cell monolayers was shown to occur 20–40 times faster than for negatively charged, COOH-modified PNP (COOH PNP) [31,32]. The primary mechanism of this PNP translocation was thought to be PNP diffusion through the BLM of the cell plasma membranes. Moreover, both COOH PNP and amidine PNP have been shown to induce ion-selective pores in planar BLM [33]. However, interactions of PNP with tBLM systems have not yet been reported. In addition the ability of the tBLM method to distinguish between polymeric ENM (e.g., PNP) based on their size and surface functionality has not yet been established.

This paper describes for the first time the characterization of interactions between a DOPC tBLM and PNP for two functional groups (COOH and amidine) and two sizes (ca. 20 and 100 nm). EIS was used to monitor changes in the tBLM's R_m following exposure to the various PNPs. Hierarchical clustering was used to confirm that the tBLM method can distinguish between PNP based on both their size and functional groups. Ultraperformance liquid chromatography–mass spectroscopy (UPLC–MS) analysis was used to explore the role of DOPC in differential aggregation of COOH PNP and amidine PNP observed after exposure to the tBLM.

2. Materials and methods

2.1. Materials

Lipids, 1,2-dipalmitoyl-*sn*-glycero-phosphothioethanol (DPPTE) and DOPC, were purchased from Avanti Polar Lipids (Alabaster, AL). Fluorescent amidine PNP (23 nm and 120 nm diameters) and fluorescent COOH PNP (20 nm and 100 nm) were purchased from Invitrogen (Eugene, Oregon). All other chemicals including sodium chloride, potassium chloride, calcium chloride and 4-(2-hydroxyethyl)-1-piperazineethanesulfonic acid (HEPES), methanol, isopropanol, acetonitrile and ammonium acetate were obtained from Sigma Aldrich (St. Louis, MO). All aqueous solutions were prepared using deionized (DI) water (18.2 MΩ) supplied by a Nanopure-UV four-stage purifier (Barnstead International, Dubuque, IA). A Sylgard 184 silicone elastomer for preparing polydimethylsiloxane (PDMS) slabs was purchased from Ellsworth Adhesives (Germantown, WI). The silver/silver chloride reference electrode and platinum counter electrode were purchased from Bioanalytical Systems (West Lafayette, IN).

2.2. Formation of tBLM on gold substrate

A tBLM was deposited on freshly cleaned gold coated silicon wafer (Lance Goddard Associates, Santa Clara, CA) in a two-step process, as described previously [26]. Briefly, a gold electrode was cleaned in fresh piranha solution (7:3 volumetric ratio of 70% H_2SO_4 and 30% H_2O_2) for 30 s, washed with deionized water and then dried in nitrogen. A self-assembled monolayer (SAM) of DPPTE was chemically adsorbed on the gold electrode to form the lower tBLM leaflet by dipping the gold substrate into 1 mM ethanolic DPPTE solution for 1 h. Then the electrode was washed with ethanol and dried in nitrogen. The SAM-coated gold electrode was incubated in 1 mM DOPC liposome solution in a PDMS slab for 24 h.

2.3. Size and surface charge characterization of PNP

Dynamic light scattering (DLS) and phase-analysis light scattering analyses were used to characterize size and surface charge of the PNP. Effective size distribution of ENM can vary significantly with medium composition, especially electrolyte concentration, due to aggregation [11,34]. Four types of PNPs were studied: 20 nm carboxylate (COOH) PNP, 100 nm COOH PNP, 23 nm amidine PNP, and 120 nm amidine PNP. The weight averaged effective diameter and zeta potential of COOH and amidine functionalized PNP were measured prior to and after interaction with a tBLM using a 90 Plus Nanoparticle Size Analyzer (Brookhaven Instruments Inc., Holtsville, NY). Dynamic and phase analysis light scattering measurements were performed at 30 °C in 10 mM and 1 mM KCl, respectively. The PNPs were ultra-sonicated for 10 min before they were exposed to the tBLM. An aliquot of the PNP was then transferred to a PDMS reservoir containing the tBLM in 10 mM KCl to give a final concentration of 100 μg/mL PNP. The area of tBLM was 0.48 cm^2.

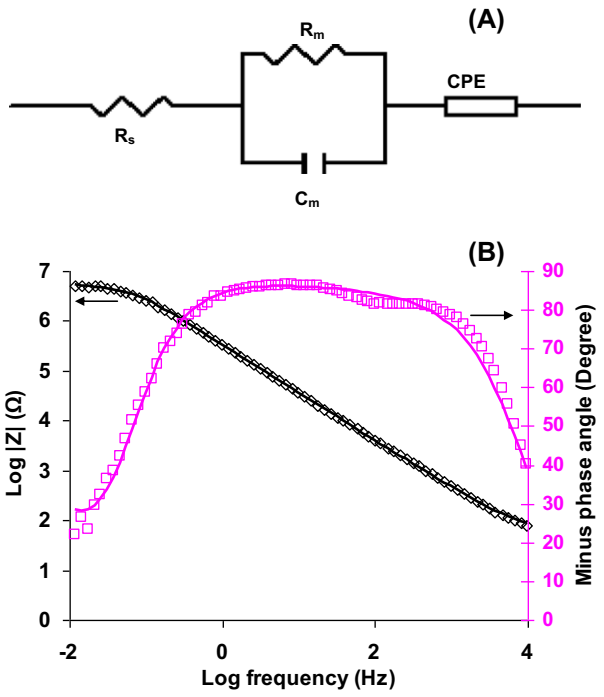

Fig. 1. (A). Modified Randles equivalent circuit that consists of an electrolyte solution resistance R_S, a membrane capacitance C_m, a membrane resistance R_m and a constant-phase element which corresponds to the hydrophilic spacer region. (B). Experimental and circuit-predicted EIS spectra of tBLM formed on 0.48 cm^2 gold. Left vertical axis: log of impedance magnitude (diamonds). Right vertical axis: minus phase angle (squares). Solid curves are impedance curves simulated by the equivalent circuit using Zview software shown in (A).

2.4. EIS characterization

EIS was performed over a frequency range of 0.01 to 10,000 Hz at 0 V bias potential relative to an Ag/AgCl reference electrode with an ac perturbation amplitude of 5 mV using a CHI660B Electrochemical Workstation (CH Instruments Inc., Austin, TX). A modified Randles equivalent circuit (Fig. 1(A)) was fit to the impedance spectra by Zview software (Scribner Associates, Southern Pines, NC). A constant phase element (CPE) was used in this modified model rather than a double layer capacitor to better explain current density distribution [35]. A CPE with two parameters, α and Q, can account for the non-uniform behavior caused by surface heterogeneity [36]. The electrochemical properties of the tBLM were measured in triplicate by EIS prior to, and after, exposure to PNP.

2.5. DOPC analysis by UPLC–MS

Ultraperformance liquid chromatography/electrospray ionization/mass spectrometry (LC/ESI/MS) analysis was used to measure DOPC in solvent extracts. A Xevo G2-S UPLC–Time of Flight MS (Waters, Milford, MA) was used in a positive electrospray ionization mode, coupled with Acquity UPLC with binary pumps. An Ascentis Express Carbon reversed phase column (100 × 2.1 mm, 2.7 μm, Sigma-Aldrich) was used to separate the DOPC lipid extract. The column temperature was kept at 30 °C, and the capillary energy was 2.14 kV. A 10-μL sample was injected through an autosampler and eluted at a flow rate of 0.4 mL/min using a mobile phase consisting of solvent A (10 mM ammonium acetate) and B (50% methanol and 50% acetonitrile) in the gradient shown in Table 1.

2.6. Statistical analysis

The tBLM's R_m vs. time profile after addition of COOH or amidine PNP was fit using a decaying exponential model, as described previously [26].

$$R_m = (R_i - R_f)\exp(bt) + R_f \quad (1)$$

$$R_m\% = (R_i - R_f)/R_i. \quad (2)$$

In this model, b is the exponential rate constant, R_i and R_f are initial and final membrane resistances, respectively, and R_m%, the fractional R_m loss that was calculated by dividing the total R_m change arising from PNP exposure by the R_i value. A pattern matrix containing a total of $n = 12$ experiments as rows and $p = 2$ features (b and R_m%) for each experiment as columns, was analyzed using hierarchical clustering procedures in R software (Version 2.13.2: The R Foundation for Statistical Computing), to evaluate the similarity between experiments. Also, Ward's method was used to determine which clusters should be linked together at each step. A difference was considered significant at $p < 0.05$ by applying two-sample t test assuming unequal variance when comparing size and surface charge of the PNP.

Table 1
Mobile phase flow gradient for UPLC–MS analysis: solvent A (10 mM ammonia acetate) and B (50% methanol and 50% acetonitrile).

Time (min)	Flow (mL/min)	%A	%B
0	0.4	30	70
20	0.4	0	100
25	0.4	0	100
25.01	0.4	30	70
28	0.4	30	70

The percentage values are given on a volumetric basis.

3. Results

3.1. Characterization of COOH and amidine PNP

Effective diameters of COOH PNP and amidine PNP were measured by DLS in 10 mM KCl (Table 2). Effective diameters of COOH PNP were 102.3 ± 1.0 nm and 20.4 ± 0.6 nm. The diameters for these PNPs given by the manufacturer (determined by transmission electron microscopy) were 100 nm and 20 nm, respectively. For amidine PNPs, the effective diameters were 93.2 ± 1.3 nm and 20.6 ± 1.5 nm, and the manufacturer-provided diameters were 120 nm and 23 nm, respectively. Based on the DLS values, a two-sample t test indicated that the size was significantly different between 20 and 100 nm COOH PNP, as well as between 23 and 120 nm amidine PNP. Also, the size of COOH PNP labeled 100 nm was significantly different from that of amidine PNP labeled as 120 nm. However, there was no significant size difference between the 20 nm COOH PNP and the 23 nm amidine PNP.

Zeta potentials of functionalized PNP (Table 3) were −32.2 ± 3.3 mV for 100 nm COOH PNP, −29.8 ± 2.1 mV for 20 nm COOH PNP, 38.3 ± 6.2 mV for 120 nm amidine PNP and 26.6 ± 3.8 mV for 23 nm amidine PNP. Based on these values, there was a significant difference in zeta potential between the two sizes of amidine PNP, but not between the two sizes of COOH PNP.

3.2. EIS characterization of tBLM

The EIS spectrum of a typical tBLM used in this study is shown as a Bode plot (logarithm phase diagram versus logarithm frequency) in Fig. 1(B). This figure has regimes dominated by different electrical characteristics: R_m-dominated in the low frequency range (<1 Hz) and capacitance-dominated in mid to high frequency range (1 Hz–1000 Hz) [37]. The equivalent circuit model fit to the impedance data had an R_m value of 2.1 MΩ cm^2 and a membrane capacitance (C_m) value 1.1 μF/cm^2. Both values are in the range reported for a highly insulating tBLM formed on a gold substrate [38,39].

3.3. Interaction of COOH and amidine PNP with tBLM

Triplicate R_m profiles from 310 min experiments were obtained for 100 nm COOH (Fig. 2(A)), 20 nm COOH PNP (Fig. 2(B)), 23 nm amidine PNP (Fig. 2(C)), and 120 nm amidine PNP (Fig. 2(D)). In these experiments, the PNPs were added immediately after the first data point was recorded. Solid lines in Fig. 2 show the best-fit exponential decay curves [26]. All PNPs tested triggered a decline in the R_m that could be described using an exponential-decay model. Based on the regression values for the b and R_m% constants (Fig. 3), the 20 nm COOH PNP reduced R_m more rapidly than the 100 nm COOH PNP did, as evidenced by a more negative b value. The smaller COOH PNP gave a greater R_m% value. Amidine PNP in both sizes reduced R_m to a plateau value, but the 120 nm amidine PNP caused a more rapid R_m decay than the 23 nm amidine PNP.

3.4. Hierarchical clustering analysis

The hierarchical clustering dendrogram (Fig. 4) for the best-fit b and R_m% constants displays the Euclidean distance between clustered

Table 2
Effective diameter of COOH and amidine PNP in 10 mM KCl measured by dynamic light scattering at 25 °C.

PNP	Effective diameter (nm)
100 nm COOH PNP	102.3 ± 1.0
20 nm COOH PNP	20.4 ± 0.6
23 nm amidine PNP	20.6 ± 1.5
120 nm amidine PNP	93.2 ± 1.3

Table 3
Zeta potential of COOH and amidine PNP in 10 mM KCl measured by phase analysis light scattering at 25 °C.

PNP	Zeta potential (mV)
100 nm COOH PNP	−32.2 ± 3.3
20 nm COOH PNP	−26.8 ± 4.8
23 nm amidine PNP	26.6 ± 3.8
120 nm amidine PNP	38.2 ± 6.2

objects as a measure of dissimilarity between samples and clusters. Samples that cluster at a smaller height are more similar (separated by less Euclidean distance) than samples that cluster at a greater height. Each set of PNP triplicates having the same size and functional surface group clustered first. Next, PNP having the same functional group but different sizes clustered. Finally, PNP having different functional groups clustered. These results demonstrate that the tBLM method, with hierarchical clustering analysis based on two experimental parameters (b and R_m%), can distinguish patterns of PNP–BLM interaction according to both functional groups and size.

3.5. Aggregation of amidine PNP

Particle size analyses (Fig. 5) showed significant increases in effective diameter during the experiments for the amidine PNP but not the COOH PNP. The increases in effective diameter for amidine PNP following tBLM exposure were accompanied by visibly apparent aggregation, as evidenced by cloudy solutions (Fig. 6(C) and (D)), while solutions containing COOH PNP remained clear (Fig. 6(A) and (B)). The effective diameter increased about 50-fold for the 23 nm amidine PNP (Fig. 5(C)), but only about 3-fold for the 120 nm amidine PNP (Fig. 5(D)). Electrolyte and buffer concentrations are known to affect the rate and extent of nanoparticle aggregation [16]. However, no aggregation was observed when the amidine PNPs were incubated in the electrolyte solution (10 mM KCl) used for the EIS experiments, indicating that electrolyte concentration was not the sole factor triggering the aggregation.

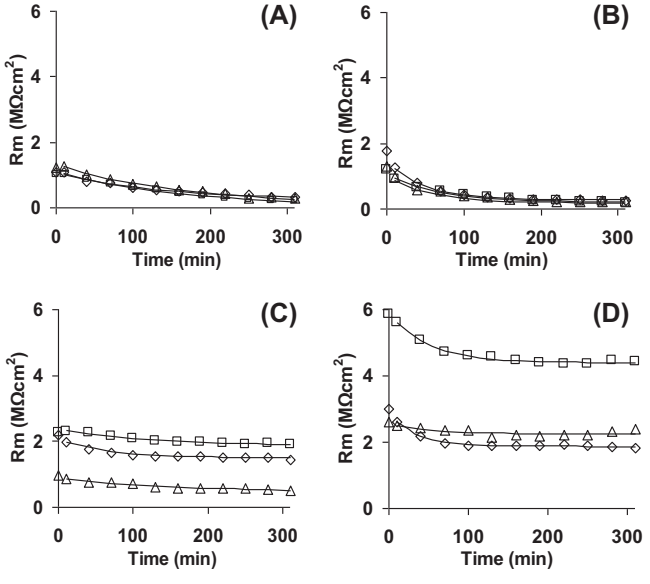

Fig. 2. R_m profiles over time during tBLM interaction with 100 μg/mL PNP in 10 mM KCl. (A): 100 nm COOH PNP, (B): 20 nm COOH PNP, (C): 23 nm amidine PNP and (D): 120 nm amidine PNP. R_m was extracted from EIS data fit by the equivalent circuit model. Three replicates were done, labeled as open diamonds, squares and triangles. All solid curves were fit by a time dependent exponential model as $R_m = (R_i - R_f)\exp(bt) + R_f$ where R_i, b and R_f represent initial R_m, rate constant and final R_m after addition of PNP.

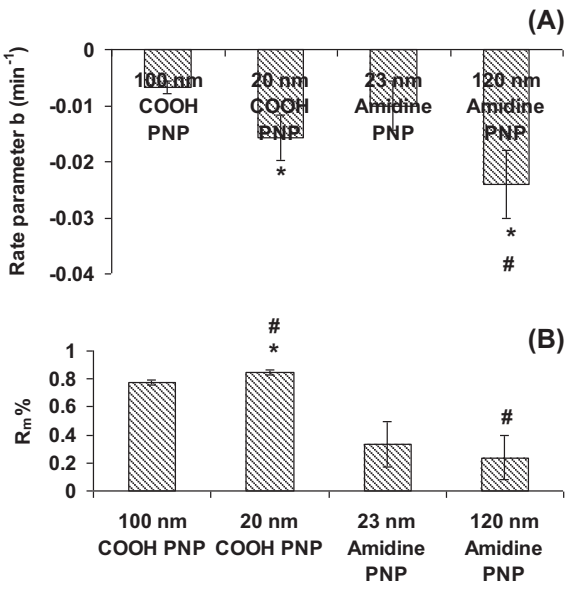

Fig. 3. Rate parameter (A) and R_m% (B) extracted using an exponential decay model and calculated from R_m profiles of COOH or amidine PNP interaction with tBLM in 10 mM KCl, respectively. The asterisk indicates statistical difference in rate parameter b or R_m% when comparing two different sizes of PNPs functionalized with either COOH or amidine. The pound sign indicates statistical difference in rate parameter b or R_m% when comparing 20 nm COOH PNP and 23 nm amidine PNP or comparing 100 nm COOH PNP and 120 nm amidine PNP.

Additional experiments were conducted to explore the involvement of PNP–BLM interactions in amidine PNP aggregation. One hypothesis was that DOPC liposomes remaining in solution after forming the upper tBLM leaflet (concentration estimated to be <1.3 μM) may have interacted with the amidine PNP, triggering aggregation. To test this hypothesis, amidine PNPs were incubated with a wide range of DOPC liposome concentrations (10, 1, 0.1, 0.01, 0.001 μM), and the size distribution profiles were measured over a 300 min period (Fig. 7). Fig. 7(A and B) show that the 23 nm amidine PNP aggregated to a lesser degree when exposed to the DOPC liposome than when exposed to a tBLM (Fig. 5C). In addition, there was no significant aggregation of 120 nm amidine PNP exposed to DOPC liposomes (Fig. 7(C) and (D)).

3.6. DOPC analysis by LC/ESI/MS

A second hypothesis to explain amidine PNP aggregation following tBLM exposure was that the PNP remove DOPC from the tBLM, and the adsorbed DOPC triggers PNP aggregation. To test this hypothesis, after the amidine PNPs were exposed to the tBLM for 5 h, the PNPs were recovered and extracted with isopropanol. The extract was then assayed for DOPC using UPLC/ESI/MS. As controls, similar extractions and assays were performed on (1) PNP-free solutions that had been contacted with a tBLM, (2) solutions containing 100 μg/mL COOH PNP that have been exposed to a DOPC tBLM, and (3) solutions containing an equivalent concentration of amidine PNP that had not been exposed to a tBLM. Fig. 8 shows the peak area of DOPC at m/z = 786.6 for the different samples, including a DOPC standard dissolved in isopropanol. The DOPC peak had a retention time of 23.08 ± 0.10 min. DOPC extracted from 120 nm and 23 nm amidine PNPs after exposure to a tBLM were at least 10 and 50 times higher, respectively, than that the highest content of DOPC detected among the controls, confirming that the amidine PNP DOPC lipids did contain DOPC following 5 h of exposure to the tBLM.

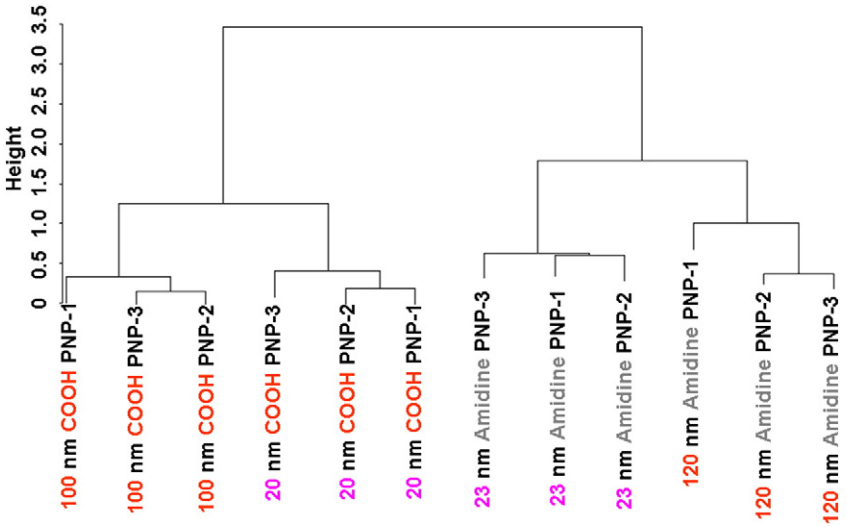

Fig. 4. Hierarchical clustering dendrogram of 20 nm and 100 nm COOH, as well as 23 nm and 120 nm amidine PNP interaction with tBLM. Distances between objects when forming the clusters were calculated by the Euclidean distance. Ward's method was used to evaluate distances between clusters and to determine which clusters should be linked together at each step.

4. Discussion

The goal of this study was to use EIS to characterize interactions between a DOPC tBLM and PNP having different sizes (ca. 20 and 100 nm) and functional groups (COOH and amidine). The hydrophobic core of an intact BLM is an excellent barrier to ion flow, resulting in high initial R_m values (on the order of 1 MΩ cm^2). The reduction in R_m following PNP exposure is likely due to PNP-induced defect (hole) formation and/or expansion. Formation and/or expansion of defects in supported BLM by dendrimers have been documented using atomic force microscopy [40,41]. Increased ion transport through these defects would be manifested as a reduction in R_m values following PNP addition, while C_m remains roughly constant [15]. Similar trends are commonly observed following incorporation of channel proteins [22] or electroactive molecules [42] into a tBLM.

Fig. 3 and 4 showed that the best-fit b values were significantly different between the two sizes of COOH PNP and also between the two sizes of amidine PNP. Moreover, the R_m% values were significantly different between the two sizes of COOH PNP. However, there was no significant difference in zeta potential between the two sizes of COOH PNP, and only a minor difference between the two sizes of amidine PNP. In addition, the PNP mass concentration was identical for all experiments (100 μg/mL). These results indicate that the tBLM method can distinguish between PNPs based on their size. The apparent size effect may be manifested indirectly, via the influence of PNP diameter on PNP surface area, PNP diffusion rate, and/or some other size-dependent influence. The importance of ENM size on biomembrane interactions has been reported previously for other types of ENM, including dendrimers [43]. The 20 nm COOH PNP triggered a more rapid decline in R_m than the 100 nm COOH PNP, consistent with other studies that reported higher trafficking or uptake rates of smaller PNP into biomembranes [31,44].

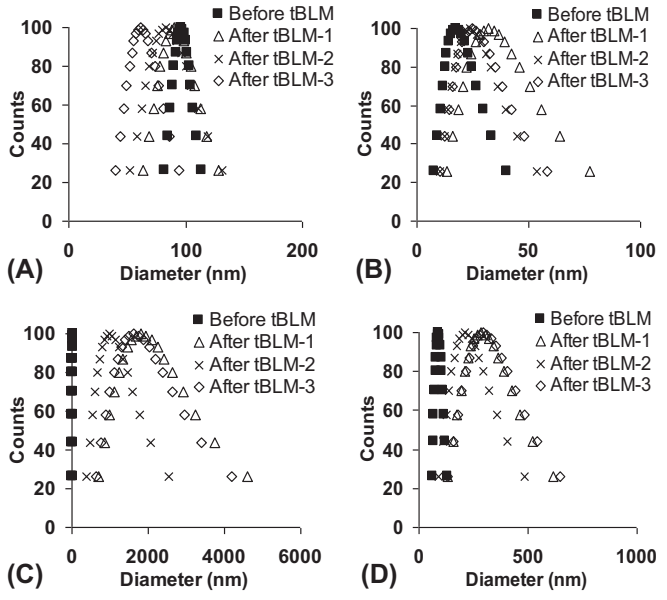

Fig. 5. Size distribution of COOH and amidine PNP in 10 mM KCl prior to and after tBLM exposure for 5 h, measured by DLS at 25 °C. (A): 100 nm COOH PNP; (B) 20 nm COOH PNP; (C): 23 nm amidine PNP and (D): 120 nm amidine PNP.

Fig. 3 and 4 also showed that the best-fit R_m% parameters were significantly different between the two functional groups for both the larger (ca. 100 nm) and smaller (ca. 20 nm) sizes. Moreover, the b values were significantly different between the functional groups for the larger PNP. The DLS-measured diameters of the 20 and 23 nm PNPs were statistically identical, and those of the 100 and 120 nm PNPs were only slightly different. These results indicate that the tBLM method can distinguish between PNPs based on their functional group. For the functional groups studied, the effect of functional group is likely manifested via surface charge. The zeta potentials differed dramatically between similarly sized COOH and amidine PNPs (Table 3).

Clustering analysis applied to the best-fit b and R_m% values also demonstrated the tBLM method's ability to distinguish between PNPs based on both size and functional group. The dendrogram (Fig. 4) indicated that the results clustered first by size and then by functional group, suggesting that functional group was the more potent variable in influencing PNP-induced tBLM disruption.

All R_m vs. time profiles were reasonably described using the exponential decay model (Eq. (1)). Although this model uses three parameters (b, R_i, and R_f), combining R_i and R_f into a single parameter (R_m%) allowed the results to be satisfactorily clustered with only two parameters.

There was a statistical difference in DOPC content associated with aggregated amidine PNP in both sizes (Fig. 8), with the smaller amidine PNP adsorbing more DOPC. This finding is consistent with aggregation for the 23 nm amidine PNP being much greater than for the 120 nm amidine PNP. While both liposomes and tBLM were able to trigger some degree of amidine ENM aggregation, tBLM exposure was far more potent in triggering aggregation than liposomes. This result may

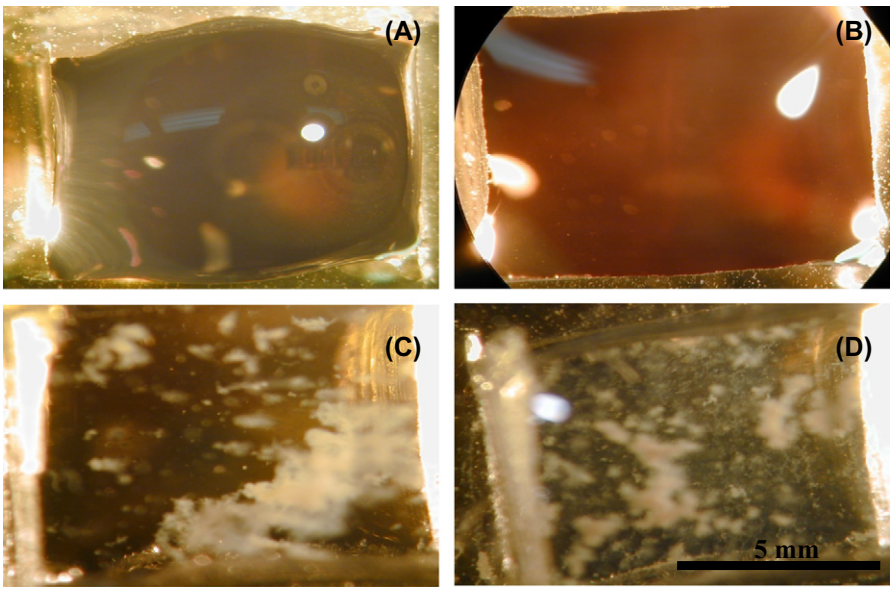

Fig. 6. Images of PDMS reservoir containing functionalized PNP after exposure to tBLM for 5 h: (A) 100 nm COOH PNP; (B) 20 nm COOH PNP; (C) 23 nm amidine PNP; (D) 120 nm amidine PNP.

reflect differences in the fluidity, geometry or lower-leaflet composition of the unsupported BLM in the liposomes compared to the tBLM.

Nanoparticles can interact with BLM through a variety of mechanisms, some of which can result in nanoparticle-induced lipid removal from the BLM [15]. Because DOPC is nearly ubiquitous, and the detection limit of the LC/MS system is extremely low (around 10^{-16} mol), harsh and complex cleaning procedures would have been required to completely remove all DOPC from the glass tubes used to extract the DOPC from PNP samples [45]. As a result, even controls to which DOPC was not added showed traces of DOPC (Fig. 8). However, the much larger amounts of DOPC found in amidine PNP samples that were exposed to the tBLM are consistent with our hypothesis that amidine PNPs extract DOPC from the tBLM. Nanoparticle-induced extraction of phospholipids from lipid bilayers has been reported by others. Tu et al. presented both experimental and theoretical evidence that graphene nanosheets can extract phospholipid from lipid bilayers and become coated by the extracted phospholipid [46]. The lipid extraction was attributed to strong dispersion interactions between the graphene and lipids. Solvent-mediated forces that can dominate nanoparticle–BLM interactions at small distances, especially for biological colloidal systems [47], may also play a role.

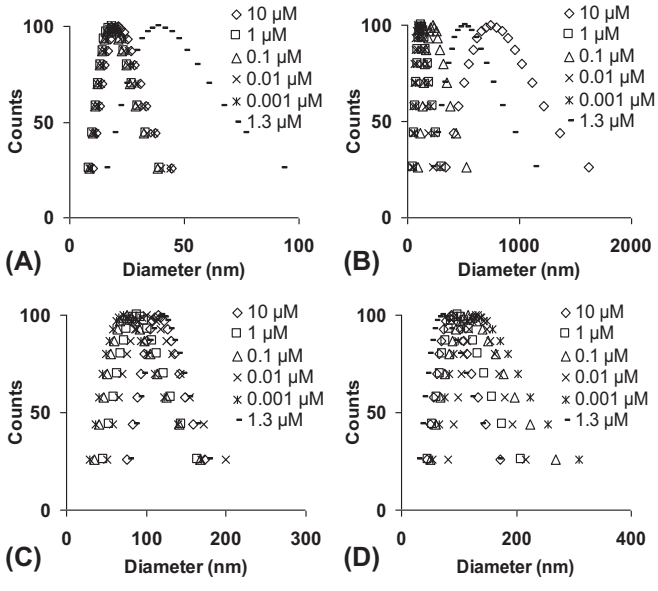

Fig. 7. Size distributions of amidine PNP at different concentrations of DOPC liposomes in 10 mM KCl, measured by DLS at 25 °C. (A): 23 nm amidine PNP at 0 min; (B) 23 nm amidine PNP at 300 min; (C): 120 nm amidine PNP at 0 min and (D): 120 nm amidine PNP at 300 min. The residue concentration of DOPC liposomes was <1.3 μM when tBLM was interacting with functionalized PNP while at all other concentrations of DOPC liposomes, amidine PNP did not contact a tBLM.

Theoretical models have predicted that nanoparticles can entirely cross a BLM and/or become wrapped in BLM [48], depending on the balance of contact-adhesion energy and curvature energies [49–51]. Simulations have estimated the minimum nanoparticle size for such wrapping to be around 30 nm, which represents the transition state between partially lipid coated nanoparticles and free nanoparticles [52]. Thus, nanoparticle size would be expected to influence the reduction of R_m following PNP exposure as was observed in Fig. 3 and 4.

Even small amounts of PNP-induced phospholipid removal from the tBLM can explain the R_m reduction shown in Fig. 2. The electrical resistivity of a BLM (about 10^{12} Ω cm) is about ten orders of magnitude higher than that of the 10 mM KCl electrolyte solution (about 70 Ω cm) [53]. As a result, the overall R_m of a high-impedance tBLM can be exquisitely sensitive to small ENM-induced defects. Assuming that a PNP-induced defect went through both the upper and lower leaflets, a defect area fraction of only 1.8×10^{-13} would cause a 50% decrease in the R_m value [26]. The amount of lipid that would need to be removed from the tBLMs used in this study to achieve this defect area fraction is less than the amount needed to fully coat a single 20 nm nanoparticle. Assuming that the PNP removed lipid only from the upper leaflet, the entire upper leaflet would need to be removed to cause a 50% reduction in R_m. The fact that R_m reductions up to about 80% of the initial value were observed in this study suggests that lipid was removed from both the top and bottom leaflets.

A second mechanism by which nanoparticles may influence R_m values is by changing the local BLM packing density. Functionalized 20 nm PNPs were shown to cause surface reconstruction of various phosphocholine BLMs in giant unilamellar vesicles [54]. Negatively charged COOH PNP induced local gelation in a DOPC BLM above the phase-transition temperature, and positively charged amidine PNP induced local fluidization in a 1,2-dipalmitoyl-*sn*-glycero-phosphocholine BLM below the phase-transition temperature [54]. In the present study,

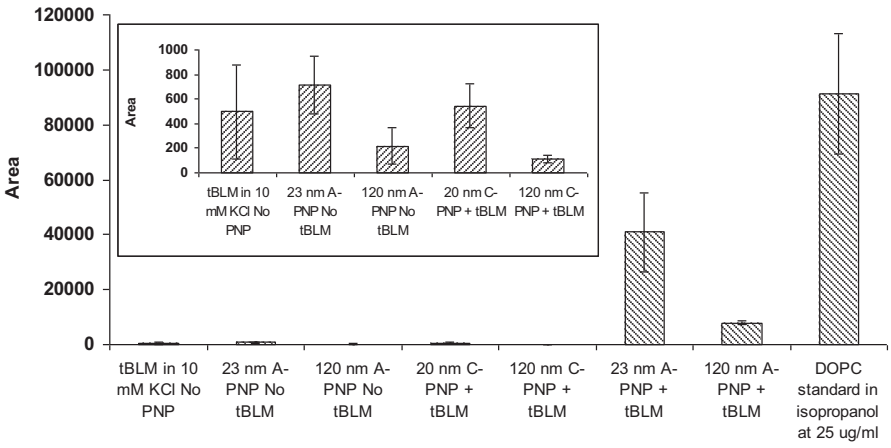

Fig. 8. Peak area of DOPC at m/z = 786.6 analyzed by UPLC–MS. DOPC lipids were extracted from functionalized PNP after exposure to tBLM and bare gold for 5 h as well as from the solution where PNP was not added in the presence of tBLM. A and C in the x axis labeled stand for amidine and COOH, respectively. The asterisk indicates statistical difference of peak area of DOPC extracted compared to the highest peak area of DOPC among five controls.

COOH PNP may have caused local DOPC gelation, but the effect of this surface reconstruction on R_m is unclear. Local PNP-induced compaction could increase the local R_m. However, unlike the giant unilamellar vesicles, which can shrink if gelation occurs [54], the tBLM has a fixed total surface area and inventory of lipids. Thus, BLM compaction in one location would cause BLM stretching in other areas, potentially creating or expanding defects, which could reduce R_m.

The finding that amidine PNP gave a smaller R_m% than the similarly sized COOH PNP (Fig. 3) was surprising, given the previous observations that (1) amidine PNP passed through primary rat alveolar epithelial cell monolayers 20–40 times faster than COOH PNP [31,32], (2) negatively charged cell membranes adsorbed cationic nanoparticles more extensively than anionic ones [55], and (3) amidine PNP more aggressively induced pores in DOPC planar BLM than COOH PNP [33]. This result is attributed to the aggregation of amidine PNP into large flocs (Fig. 5 and 6), which significantly depleted the effective PNP concentration in the solution.

The PNP's surface functional group was found to strongly influence the aggregation rate during tBLM exposure. This finding is consistent with our previous observation that bare silica nanoparticles exposed to a DOPC tBLM aggregated significantly (10− fold increase in effective diameter), while COOH-functionalized silica nanoparticles having a similar zeta potential did not [26]. In that study, control experiments provided strong evidence that the factor triggering aggregation of the bare silica nanoparticles was exposure to the tBLM. The different aggregation properties of the amidine and COOH PNPs may be interpreted in terms of long-range charge interactions. The PNP's surface charge generates an electrostatic repulsive force that provides an energy barrier to PNP collision and aggregation. Electrolytes that shield the charge or compounds that adsorb onto the PNP's surface can reduce the repulsive force, thereby accelerating aggregation [56,57]. Previous studies to characterize PNP aggregation under reaction-limited [58] and diffusion-limited [59] conditions showed that even trace quantities of surface-active impurities can significantly increase PNP aggregation rates. For example, low concentrations of hydrophobically modified ethyl(hydroxyethyl)cellulose polymer and sodium dodecyl sulfate triggered a rapid aggregation of cationic PNP into macroscopic flocs similar to those shown in Fig. 6 [60]. The authors proposed that the amphiphilic polymer adsorbed onto the PNP, creating high-energy hydrophobic patches on the PNP surface. Spontaneous bridging between such hydrophobic patches on adjacent PNP would be entropically driven. Highly ordered water clathrates form adjacent to hydrophobic patches in aqueous solution. Bridging of two hydrophobic patches would eliminate the clathrates, thereby increasing the system's entropy [61]. A similar mechanism is likely to occur in the PNP–tBLM system. Extraction of small quantities of DOPC from the tBLM would create hydrophobic monolayer patches on the PNPs' surfaces. Bridging of patches between adjacent nanoparticles would form PNP clusters, and then bridging between clusters would form the flocs seen in Fig. 6.

The type of BLM system used (tBLM vs planar BLM) also affected the aggregation rate of amidine PNP during exposure to a DOPC BLM. The heavy aggregation observed for amidine PNP (Fig. 6) was not observed when the same amidine PNPs were exposed to a DOPC planar BLM [33]. We attribute this difference to physical constraints that the gold electrode places on PNP penetration into the tBLM. Amidine and COOH PNPs have been shown to pass through cell membranes, reportedly by diffusion through the plasma membrane [31,32]. In the process, the PNPs are likely to become coated with a BLM, as has been described for other types of nanoparticles, including dendrimers [62]. BLM-coated PNP would be expected to be relatively stable against aggregation, as are BLM-coated silica nanoparticles (e.g., TRANSIL®) [63].

This conceptual model of how PNPs interact differently with a tBLM than with a planar BLM is also consistent with trends in the electrochemical results. For the planar BLM, DOPC molecules removed by the PNP would be replaced from the Plateau–Gibbs border. Each of the observed transient current spikes that interrupt extended periods of low background current [33] could result from a pore formed as a PNP penetrates into the planar BLM, followed by the flow of lipids from the Plateau–Gibbs border to seal the pore and terminate the current spike. In contrast to the planar BLM, the tBLM's underlying gold electrode limits the PNP's penetration depth into the tBLM. Also, tethering of some lipids to the gold electrode limits the amount of lipid that can be extracted from the lower leaflet and consequently the degree of R_m reduction observed following PNP exposure. Consequently, amidine PNP would likely only become partially coated with phospholipid after contacting the tBLM. Monolayer lipid patches would be hydrophobic and facilitate the observed interparticle bridging and aggregation. In support of this model, significant lipid removal from supported BLM by cationic nanoparticles, including dendrimers, poly-L-lysine, polyethylenimine, and diethylaminoethyl-dextran, has been reported [40,41,64]. Such lipid removal would generate patches of bare electrode or lipid monolayer whose impedance would be lower than the bilayer, resulting in the reductions in R_m seen in Fig. 2.

Based on this conceptual model, the amount of lipid removed from the tBLM, and hence the observed degree of reduction of R_m, would be expected to depend on the nanoparticle's size. The maximum depth to which the PNP could penetrate into the tBLM is equal to the tBLM's depth (about 5 nm). However, the total surface area of the PNP's spherical cap in contact with the tBLM at the maximum penetration depth, as well as the fraction of the nanoparticle's surface area in contact with the

tBLM, would vary with the nanoparticle's size, consistent with the tBLM method's observed ability to discern differences in PNP particle size.

Comparison of results from the tBLM and pBLM systems provides insight into the relative advantages, disadvantages, and areas of complementarity of the two methods. Both methods are based on a BLM having an area-normalized resistance on the order of 1 MΩ cm^2. Because the planar BLM is unsupported, it is fragile and prone to rupture during several-hour experiments, whereas the tBLM's tethered lower leaflet makes it more physically robust. Microscopic roughness of the gold electrode's surface causes slight defects in the tBLM, resulting in initial area-normalized R_m values that are slightly less than those for planar BLM and prone to minor variations between replicates. In control experiments conducted without nanoparticle addition, the tBLM's R_m was constant over a several-hour period with a random fluctuation level of 0.062 MΩ cm^2 at a 95% confidence interval [26]. The noise level of the planar BLM is about 1 pA. PNP interactions with a planar BLM induced pores, as evidenced by sudden increases in current that were at times one or more orders of magnitude greater than the background signal [33]. In contrast, PNP interactions with the tBLM reduced R_m over a smaller range (about 80% of the initial value). The lower sensitivity for the tBLM method is due in part to differences in the measurement methods. The planar BLM method uses chronoamperometry, which measures increases in current against an initially low value, whereas the tBLM method uses EIS, which measures decreases in tBLM resistance against an initially high value. In addition, chemical tethering of the lower tBLM leaflet makes it difficult to form a sizable pore through both leaflets. Because of these inherent differences, direct quantitative comparison of results from the tBLM and the planar BLM methods is difficult.

However, application of both the tBLM and planar BLM methods to the same ENM (e.g., COOH and amidine PNP) and phospholipid (e.g., DOPC) provides complementary information that can help elucidate interaction mechanisms. The planar BLM provides sensitive, time-resolved information about single-pore events with a time constant on the milliseconds. For example, penetration of a nanoparticle through the planar BLM, followed by rapid resealing of the BLM is consistent with the frequently observed current spikes [33]. However, nanoparticle-induced lipid removal is difficult to discern with the planar BLM method, because the Plateau-Gibbs border quickly replaces the removed lipids, allowing the pore to close. In contrast, the fixed area and lipid inventory of the tBLM method does not allow lipid replacement, so ENM-induced extraction of lipids from the tBLM permanently reduces R_m. Thus, the tBLM system provides a global measure of the ENM's influence on the tBLM's R_m that is integrated over time and area and has a time constant ranging from seconds to hours. The tBLM method is more robust than the planar BLM method. In our experience, some nanoparticles are particularly aggressive toward planar BLM, causing rapid rupture and then preventing the BLM from being reestablished. In addition, the equipment cost and technical difficulty of tBLM experiments are less for the tBLM system than those for the planar bilayer system. However, further experimental and modeling research is needed to map time-dependent changes in R_m obtained using the tBLM method into a mechanistic understanding of ENM–biomembrane molecular interactions.

5. Conclusions

This paper demonstrates for the first time that the tBLM method can measure biomembrane disruption by PNP with sensitivity that can discriminate between PNPs having the same functional groups but different sizes, and between PNPs having the same size but different functional groups. Both PNP sizes tested (ca. 20 and 100 nm) and both functional groups (amidine and COOH) resulted in reductions in R_m that could be described by a simple exponential decay model. Statistical analysis of two regression parameters from the exponential model (b and R_m%) yielded a dendrogram that first clustered the triplicates for all test cases, then clustered PNPs having the same functional group but different sizes, and finally clustered the PNPs having different functional groups. These results further established the tBLM method as a sensitive and versatile tool to characterize ENM–biomembrane interactions. The simple and well-characterized tBLM interface can be easily customized by changing the lipid composition, adding additional biomolecules, etc., to test a broad range of hypotheses. The information-rich R_m vs. time profiles are likely to contain additional insight into fundamental mechanisms by which ENM interact with biomembranes that could be discerned through further studies and integration of mathematical models. The finding that amidine PNPs aggregate in the presence of tBLM but not planar BLM or intact cell membranes suggests that the tBLM method provides complementary information to the other experimental platforms. The presence of DOPC lipids associated with amidine PNP aggregates after exposure to the tBLM is consistent with the hypothesis that amidine PNPs capture lipids from the tBLM, and that the captured lipids trigger aggregation. The utility of the tBLM method to characterize ENM–biomembrane interactions, combined with its ability to be miniaturized and adapted with MEMS systems, may lead to automated, high-throughput screening systems to identify ENM that are both safe and effective for the desired applications.

Acknowledgements

This research was financially supported by NIH 5RC2ES018756-02. We thank the Research Technology Support Facility in Michigan State University regarding the UPLC–MS analysis.

References

[1] J.F. Hicks, D.T. Miles, R.W. Murray, Quantized double-layer charging of highly monodisperse metal nanoparticles, J. Am. Chem. Soc. 124 (2002) 13322–13328.
[2] N.J. Walker, J.R. Bucher, A 21st century paradigm for evaluating the health hazards of nanoscale materials? Toxicol. Sci. 110 (2009) 251–254.
[3] V. Stone, K. Donaldson, Nanotoxicology: signs of stress, Nat. Nanotechnol. 1 (2006) 23–24.
[4] D.B. Warheit, Debunking some misconceptions about nanotoxicology, Nano Lett. 10 (2010) 4777–4782.
[5] A. Nel, T. Xia, L. Madler, N. Li, Toxic potential of materials at the nanolevel, Science 311 (2006) 622–627.
[6] C. Buzea, I.I. Pacheco, K. Robbie, Nanomaterials and nanoparticles: sources and toxicity, Biointerphases 2 (2007) MR17–MR71.
[7] A.D. Maynard, R.J. Aitken, T. Butz, V. Colvin, K. Donaldson, G. Oberdorster, M.A. Philbert, J. Ryan, A. Seaton, V. Stone, S.S. Tinkle, L. Tran, N.J. Walker, D.B. Warheit, Safe handling of nanotechnology, Nature 444 (2006) 267–269.
[8] J. McCarthy, X. Gong, D. Nahirney, M. Duszyk, M. Radomski, Polystyrene nanoparticles activate ion transport in human airway epithelial cells, Int. J. Nanomedicine 6 (2011) 1343–1356.
[9] Y. Liu, W. Li, F. Lao, Y. Liu, L. Wang, R. Bai, Y. Zhao, C. Chen, Intracellular dynamics of cationic and anionic polystyrene nanoparticles without direct interaction with mitotic spindle and chromosomes, Biomaterials 32 (2011) 8291–8303.
[10] T. Xia, M. Kovochich, M. Liong, J.I. Zink, A.E. Nel, Cationic polystyrene nanosphere toxicity depends on cell-specific endocytic and mitochondrial injury pathways, ACS Nano 2 (2007) 85–96.
[11] G. Oberdorster, A. Maynard, K. Donaldson, V. Castranova, J. Fitzpatrick, K. Ausman, J. Carter, B. Karn, W. Kreyling, D. Lai, S. Olin, N. Monteiro-Riviere, D. Warheit, H. Yang, A.r.f.t.I.R.F.R.S.I.N.T.S.W. Group, principles for characterizing the potential human health effects from exposure to nanomaterials: elements of a screening strategy, Part. Fibre Toxicol. 2 (2005) 8.
[12] A. Baun, N.B. Hartmann, K. Grieger, K.O. Kusk, Ecotoxicity of engineered nanoparticles to aquatic invertebrates: a brief review and recommendations for future toxicity testing, Ecotoxicology 17 (2008) 387–395.
[13] J.C. Bonner, R.M. Silva, A.J. Taylor, J.M. Brown, S.C. Hilderbrand, V. Castranova, D. Porter, A. Elder, G. Oberdorster, J.R. Harkema, L.A. Bramble, T.J. Kavanagh, D. Botta, A. Nel, K.E. Pinkerton, Interlaboratory evaluation of rodent pulmonary responses to engineered nanomaterials: the NIEHS Nano GO Consortium, Environ. Health Perspect. 121 (2013) 676–682.
[14] T. Xia, R.F. Hamilton, J.C. Bonner, E.D. Crandall, A. Elder, F. Fazlollahi, T.A. Girtsman, K. Kim, S. Mitra, S.A. Ntim, G. Orr, M. Tagmount, A.J. Taylor, D. Telesca, A. Tolic, C.D. Vulpe, A.J. Walker, X. Wang, F.A. Witzmann, N.Q. Wu, Y.M. Xie, J.I. Zink, A. Nel, A. Holian, Interlaboratory evaluation of in vitro cytotoxicity and inflammatory responses to engineered nanomaterials: The NIEHS Nano GO Consortium, Environ. Health Perspect. 121 (2013) 683–690.
[15] A. Negoda, Y. Liu, W.-C. Hou, C. Corredor, Y.B. Moghadam, C. Musolff, L. Li, W. Walker, P. Westerhoff, J.A. Mason, P. Duxbury, D.J. Posner, R.M. Worden, Engineered nanomaterial interactions with bilayer lipid membranes: screening platforms to assess nanoparticle toxicity, Int. J. Biomed. Nanosci. Nanotechnol. 3 (2013) 32.

[16] R.C. Murdock, L. Braydich-Stolle, A.M. Schrand, J.J. Schlager, S.M. Hussain, Characterization of nanomaterial dispersion in solution prior to in vitro exposure using dynamic light scattering technique, Toxicol. Sci. 101 (2008) 239–253.
[17] H. Fritz, M. Maier, E. Bayer, Cationic polystyrene nanoparticles: preparation and characterization of a model drug carrier system for antisense oligonucleotides, J. Colloid Interface Sci. 195 (1997) 272–288.
[18] A.E. Nel, L. Madler, D. Velegol, T. Xia, E.M.V. Hoek, P. Somasundaran, F. Klaessig, V. Castranova, M. Thompson, Understanding biophysicochemical interactions at the nano-bio interface, Nat. Mater. 8 (2009) 543–557.
[19] P.J. Borm, D. Robbins, S. Haubold, T. Kuhlbusch, H. Fissan, K. Donaldson, R. Schins, V. Stone, W. Kreyling, J. Lademann, J. Krutmann, D. Warheit, E. Oberdorster, The potential risks of nanomaterials: a review carried out for ECETOC, Part. Fibre Toxicol. 3 (2006) 11.
[20] L.C. Cheng, X.M. Jiang, J. Wang, C.Y. Chen, R.S. Liu, Nano-bio effects: interaction of nanomaterials with cells, Nanoscale 5 (2013) 3547–3569.
[21] G. Krishna, J. Schulte, B.A. Cornell, R.J. Pace, P.D. Osman, Tethered bilayer membranes containing ionic reservoirs: selectivity and conductance, Langmuir 19 (2003) 2294–2305.
[22] R. Naumann, D. Walz, S.M. Schiller, W. Knoll, Kinetics of valinomycin-mediated K^+ ion transport through tethered bilayer lipid membranes, J. Electroanal. Chem. 550 (2003) 241–252.
[23] D.J. McGillivray, G. Valincius, F. Heinrich, J.W. Robertson, D.J. Vanderah, W. Febo-Ayala, I. Ignatjev, M. Losche, J.J. Kasianowicz, Structure of functional *Staphylococcus aureus* alpha-hemolysin channels in tethered bilayer lipid membranes, Biophys. J. 96 (2009) 1547–1553.
[24] S.R. Jadhav, R.M. Worden, Interaction of Polyamidoamine (PAMAM) Nanoparticles With the Glassy Carbon Supported Bilayer Lipid Membrane, NSTI 2008, NSTI, Boston, MA, 2008.
[25] P.N. Yaron, B.D. Holt, P.A. Short, M. Losche, M.F. Islam, K.N. Dahl, Single wall carbon nanotubes enter cells by endocytosis and not membrane penetration, J. Nanobiotechnol. 9 (2011) 45.
[26] Y. Liu, Z. Zhang, Q. Zhang, G.L. Baker, R.M. Worden, Biomembrane disruption by silica-core nanoparticles: effect of surface functional group measured using a tethered bilayer lipid membrane, Biochim. Biophys. Acta Biomembr. 1838 (2014) 429–437.
[27] H.C. Tian, J. Zhou, B. Qiao, Y. Liu, J.M. Xia, Y.J. Yuan, Lipidome profiling of *Saccharomyces cerevisiae* reveals pitching rate-dependent fermentative performance, Appl. Microbiol. Biotechnol. 87 (2010) 1507–1516.
[28] G.J. Mahler, M.B. Esch, E. Tako, T.L. Southard, S.D. Archer, R.P. Glahn, M.L. Shuler, Oral exposure to polystyrene nanoparticles affects iron absorption, Nat. Nanotechnol. 7 (2012) 264–271.
[29] E. Acosta, Bioavailability of nanoparticles in nutrient and nutraceutical delivery, Curr. Opin. Colloid Interface Sci. 14 (2009) 3–15.
[30] R. Singh, J.W. Lillard Jr., Nanoparticle-based targeted drug delivery, Exp. Mol. Pathol. 86 (2009) 215–223.
[31] N.R. Yacobi, L. Demaio, J. Xie, S.F. Hamm-Alvarez, Z. Borok, K.J. Kim, E.D. Crandall, Polystyrene nanoparticle trafficking across alveolar epithelium, Nanomedicine 4 (2008) 139–145.
[32] N.R. Yacobi, N. Malmstadt, F. Fazlollahi, L. DeMaio, R. Marchelletta, S.F. Hamm-Alvarez, Z. Borok, K.J. Kim, E.D. Crandall, Mechanisms of alveolar epithelial translocation of a defined population of nanoparticles, Am. J. Respir. Cell Mol. Biol. 42 (2010) 604–614.
[33] A. Negoda, K.-J. Kim, E.D. Crandall, R.M. Worden, Polystyrene nanoparticle exposure induces ion-selective pores in lipid bilayers, Biochim. Biophys. Acta Biomembr. 1828 (2013) 2215–2222.
[34] D.B. Warheit, How meaningful are the results of nanotoxicity studies in the absence of adequate material characterization? Toxicol. Sci. 101 (2008) 183–185.
[35] G.J. Brug, A.L.G. van den Eeden, M. Sluyters-Rehbach, J.H. Sluyters, The analysis of electrode impedances complicated by the presence of a constant phase element, J. Electroanal. Chem. Interfacial Electrochem. 176 (1984) 275–295.
[36] Z. Lukacs, Evaluation of model and dispersion parameters and their effects on the formation of constant-phase elements in equivalent circuits, J. Electroanal. Chem. 464 (1999) 68–75.
[37] S. Alonso-Romanowski, L.M. Gassa, J.R. Vilche, An investigation by EIS of gramicidin channels in bilayer lipid membranes, Electrochim. Acta 40 (1995) 1561–1567.
[38] E. Sackmann, Supported membranes: scientific and practical applications, Science 271 (1996) 43–48.
[39] A.L. Plant, M. Gueguetchkeri, W. Yap, Supported phospholipid/alkanethiol biomimetic membranes: insulating properties, Biophys. J. 67 (1994) 1126–1133.
[40] S. Hong, A.U. Bielinska, A. Mecke, B. Keszler, J.L. Beals, X. Shi, L. Balogh, B.G. Orr, J.R. Baker Jr., M.M. Banaszak Holl, Interaction of poly(amidoamine) dendrimers with supported lipid bilayers and cells: hole formation and the relation to transport, Bioconjug. Chem. 15 (2004) 774–782.
[41] J. Chen, J.A. Hessler, K. Putchakayala, B.K. Panama, D.P. Khan, S. Hong, D.G. Mullen, S.C. DiMaggio, A. Som, G.N. Tew, A.N. Lopatin, J.R. Baker, M.M.B. Holl, B.G. Orr, Cationic nanoparticles induce nanoscale disruption in living cell plasma membranes, J. Phys. Chem. B 113 (2009) 11179–11185.
[42] R. Campos, R. Kataky, Electron transport in supported and tethered lipid bilayers modified with bioelectroactive molecules, J. Phys. Chem. B 116 (2012) 3909–3917.
[43] P.R. Leroueil, S. Hong, A. Mecke, J.R. Baker, B.G. Orr, M.M. Banaszak Holl, Nanoparticle interaction with biological membranes: does nanotechnology present a Janus face? Acc. Chem. Res. 40 (2007) 335–342.
[44] H.J. Johnston, M. Semmler-Behnke, D.M. Brown, W. Kreyling, L. Tran, V. Stone, Evaluating the uptake and intracellular fate of polystyrene nanoparticles by primary and hepatocyte cell lines in vitro, Toxicol. Appl. Pharmacol. 242 (2010) 66–78.
[45] M.M. Angrish, A.D. Jones, J.R. Harkema, T.R. Zacharewski, Aryl hydrocarbon receptor-mediated induction of Stearoyl-CoA desaturase 1 alters hepatic fatty acid composition in TCDD-elicited steatosis, Toxicol. Sci. 124 (2011) 299–310.
[46] Y. Tu, M. Lv, P. Xiu, T. Huynh, M. Zhang, M. Castelli, Z. Liu, Q. Huang, C. Fan, H. Fang, R. Zhou, Destructive extraction of phospholipids from *Escherichia coli* membranes by graphene nanosheets, Nat. Nanotechnol. 8 (2013) 594–601.
[47] B.W. Ninham, Long-range vs. short-range forces. The present state of play, J. Phys. Chem. 84 (1980) 1423–1430.
[48] R. Lipowsky, H.-G. Döbereiner, Vesicles in contact with nanoparticles and colloids, Europhys. Lett. 43 (1998) 6.
[49] A.H. Bahrami, M. Raatz, J. Agudo-Canalejo, R. Michel, E.M. Curtis, C.K. Hall, M. Gradzielski, R. Lipowsky, T.R. Weikl, Wrapping of nanoparticles by membranes, Adv. Colloid Interf. Sci. 208 (2014) 214–224.
[50] M. Deserno, W.M. Gelbart, Adhesion and wrapping in colloid–vesicle complexes, J. Phys. Chem. B 106 (2002) 5543–5552.
[51] M. Deserno, T. Bickel, Wrapping of a spherical colloid by a fluid membrane, Europhys. Lett. 62 (2003) 767–774.
[52] Y. Roiter, M. Ornatska, A.R. Rammohan, J. Balakrishnan, D.R. Heine, S. Minko, Interaction of nanoparticles with lipid membrane, Nano Lett. 8 (2008) 941–944.
[53] T. Cassier, A. Sinner, A. Offenhäuser, H. Möhwald, Homogeneity, electrical resistivity and lateral diffusion of lipid bilayers coupled to polyelectrolyte multilayers, Colloids Surf. B: Biointerfaces 15 (1999) 215–225.
[54] B. Wang, L. Zhang, S.C. Bae, S. Granick, Nanoparticle-induced surface reconstruction of phospholipid membranes, Proc. Natl. Acad. Sci. 105 (2008) 18171–18175.
[55] A. Verma, F. Stellacci, Effect of surface properties on nanoparticle–cell interactions, Small 6 (2010) 12–21.
[56] M.Y. Lin, H.M. Lindsay, D.A. Weitz, R.C. Ball, R. Klein, P. Meakin, Universality in colloid aggregation, Nature 339 (1989) 360–362.
[57] M.J. Snowden, B. Vincent, The temperature-controlled flocculation of crosslinked latex particles, J. Chem. Soc. Chem. Commun. (1992) 1103–1105.
[58] M.Y. Lin, H.M. Lindsay, D.A. Weitz, R.C. Ball, R. Klein, P. Meakin, Universal reaction-limited colloid aggregation, Phys. Rev. A 41 (1990) 2005–2020.
[59] M.Y. Lin, H.M. Lindsay, D.A. Weitz, R. Klein, R.C. Ball, P. Meakin, Universal diffusion-limited colloid aggregation, J. Phys. Condens. Matter 2 (1990) 3093–3113.
[60] R.A. Lauten, A.L. Kjoniksen, B. Nystrom, Colloid polymer interactions and aggregation in aqueous mixtures of polystyrene latex, sodium dodecyl sulfate, and a hydrophobically modified polymer: a dynamic light scattering study, Langmuir 17 (2001) 924–930.
[61] M.J. Madou, From MEMS to Bio-MEMS and Bio-NEMS: Manufacturing Techniques and Applications, III ed. CRC Press, 2011.
[62] A. Mecke, I.J. Majoros, A.K. Patri, J.R. Baker Jr., M.M. Holl, B.G. Orr, Lipid bilayer disruption by polycationic polymers: the roles of size and chemical functional group, Langmuir 21 (2005) 10348–10354.
[63] A. Loidl-Stahlhofen, T. Hartmann, M. Schottner, C. Rohring, H. Brodowsky, J. Schmitt, J. Keldenich, Multilamellar liposomes and solid-supported lipid membranes (TRANSIL): screening of lipid–water partitioning toward a high-throughput scale, Pharm. Res. 18 (2001) 1782–1788.
[64] S. Hong, P.R. Leroueil, E.K. Janus, J.L. Peters, M.-M. Kober, M.T. Islam, B.G. Orr, J.R. Baker, M.M. Banaszak Holl, Interaction of polycationic polymers with supported lipid bilayers and cells: nanoscale hole formation and enhanced membrane permeability, Bioconjug. Chem. 17 (2006) 728–734.